Astronomy & Astrophysics manuscript no. h˙nindos6
November 21, 2005

What is the spatial distribution of magnetic helicity injected in a solar active region?

E. Pariat[1], A. Nindos[2], P. Démoulin[1], and M.A. Berger[3]

[1] Observatoire de Paris, LESIA, UMR 8109 (CNRS), F-92195 Meudon Principal Cedex, France e-mail: Etienne.Pariat@obspm.fr,pascal.demoulin@obspm.fr
[2] Section of Astrogeophysics, Department of Physics, University of Ioannina GR-45110, Greece e-mail: anindos@cc.uoi.gr
[3] Department of Mathematics, University College London e-mail: m.berger@ucl.ac.uk

Received ; accepted

ABSTRACT

Context. Magnetic helicity is suspected to play a key role in solar phenomena such as flares and coronal mass ejections. Several investigations have recently computed the photospheric flux of magnetic helicity in active regions. The derived spatial maps of the helicity flux density, called G_A, have an intrinsic mixed-sign patchy distribution.
Aims. Pariat et al. (2005) recently showed that G_A is only a proxy of the helicity flux density, which tends to create spurious polarities. They proposed a better proxy, G_θ. We investigate here the implications of this new approach on observed active regions.
Methods. The magnetic data are from MDI/SoHO instrument and the photospheric velocities are computed by local correlation tracking. Maps and temporal evolution of G_A and G_θ are compared using the same data set for 5 active regions.
Results. Unlike the usual G_A maps, most of our G_θ maps show almost unipolar spatial structures because the nondominant helicity flux densities are significantly suppressed. In a few cases, the G_θ maps still contain spurious bipolar signals. With further modelling we infer that the real helicity flux density is again unipolar. On time-scales larger that their transient temporal variations, the time evolution of the total helicity fluxes derived from G_A and G_θ show small differences. However, unlike G_A, with G_θ the time evolution of the total flux is determined primarily by the predominant-signed flux while the nondominant-signed flux is roughly stable and probably mostly due to noise.
Conclusions. Our results strongly support the conclusion that the spatial distribution of helicity injected into active regions is much more coherent than previously thought: on the active region scale the sign of the injected helicity is predominantly uniform. These results have implications for the generation of the magnetic field (dynamo) and for the physics of both flares and coronal mass ejections.

Key words. 06.13.1 Sun: magnetic fields, 06.16.2 Sun: photosphere, 06.03.02 Sun: Corona

1. Introduction

1.1. Interest of magnetic helicity

Magnetic helicity quantifies how the magnetic field is sheared and/or twisted compared to its lowest energy state, the potential field. Observations of the solar atmosphere show the existence of several sheared, even helical-like magnetic structures. Such structures are often associated with flares, eruptive filaments and coronal mass ejections (CMEs). Magnetic helicity thus appears as a key element in a large number of coronal phenomena and the computation of magnetic helicity is a very important task in solar physics. Therefore, it is not surprising that recently significant new developments have been made in the subject (see reviews in Brown et al. 1999; Berger 2003).

For a divergence-free field $\mathbf{B}$ within a bounded volume $\mathcal{V}$ of surface $\mathcal{S}$ where the normal component $B_n = \mathbf{B}\cdot\hat{\boldsymbol{n}}$ on $\mathcal{S}$ is not null (i.e. like the situation in the solar corona), Berger & Field (1984) have defined a relative magnetic helicity, H. H is defined by subtracting the helicity of a reference field having the same normal component B_n on $\mathcal{S}$ as $\mathbf{B}$. Using a potential field, $\mathbf{B}_p$, is a convenient choice for a reference field. An expression for H, valid for any gauge is (Finn & Antonsen 1985):

$$H = \int_{\mathcal{V}} (\mathbf{A} + \mathbf{A}_p) \cdot (\mathbf{B} - \mathbf{B}_p)\ \mathrm{d}^3x\,. \qquad (1)$$

with $\mathbf{A}$ the vector potential, satisfying $\mathbf{B} = \boldsymbol{\nabla} \times \mathbf{A}$ and $\mathbf{A}_p$ is the vector potential of the potential field.

Send offprint requests to: E. Pariat

The direct computation of the helicity in the corona requires knowledge of the magnetic field in the entire volume, but measurements are simplest at the photospheric level; thus one of the best ways to estimate magnetic helicity is by integrating in time the helicity flux injected through the photosphere (e.g. Chae 2001; Chae et al. 2001, 2004; Kusano et al. 2002, 2004a,b; Maeshiro et al. 2005; Moon et al. 2002a,b, 2003a,b; Nindos & Zhang 2002; Nindos et al. 2003; Yamamoto et al. 2005; Yokoyama et al. 2003). Several studies have shown an intimate association between eruptive events and variations of helicity injection. Kusano et al. (2004b) suggested that solar flares can be initiated by reversal of magnetic shear, *i.e*, annihilation of magnetic helicity (Kusano et al. 2003). This idea mainly comes from observations of the structure of helicity injection in active regions. The helicity flux density maps appear to be spatially and temporally extremely complicated, with simultaneous and adjacent polarities of both signs of helicity density (Chae 2001; Moon et al. 2002a; Kusano et al. 2002; Nindos et al. 2003; Maeshiro et al. 2005). But is the usual definition of the helicity flux density correct?

1.2. Helicity flux

Using the gauge $\boldsymbol{\nabla} \cdot \mathbf{A}_p = 0$, and selecting the boundary condition $\mathbf{A}_p \cdot \hat{\mathbf{n}} = 0$ for the vector potential of the potential (reference) field, Berger & Field (1984), derived the flux of magnetic helicity through the surface, in particular the solar photosphere:

$$\frac{\mathrm{d}H}{\mathrm{d}t} = 2 \int_{\mathcal{S}} [(\mathbf{A}_p \cdot \mathbf{B}) v_n - (\mathbf{A}_p \cdot \mathbf{v}) B_n] \; \mathrm{d}\mathcal{S} \qquad (2)$$

where $\mathbf{v}$ is the plasma velocity. The first term corresponds to the injection of magnetic helicity by advection whereas the second term is the flux of helicity due to motions parallel to $\mathcal{S}$.

In order to estimate $\mathrm{d}H/\mathrm{d}t$ from observations one should determine the velocity field $\mathbf{v}$ and the magnetic field $\mathbf{B}$ on the photosphere. Presently, the horizontal velocity field is derived by applying the local correlation tracking (LCT) method to follow explicitly the magnetic fluxes, using time sequence of longitudinal magnetograms. Since only horizontal velocities are deduced from the temporal evolution of B_n, it has been believed that only the shear term could be derived (e.g. Chae et al. 2001; Nindos & Zhang 2002; Moon et al. 2002b). However, when using the LCT method one estimates the flux tube velocity $\mathbf{u}$ parallel to $\mathcal{S}$, and not the plasma velocity, $\mathbf{v}$: the velocity derived from the LCT method can be expressed as (Démoulin & Berger 2003):

$$\mathbf{u} = \mathbf{v}_t - \frac{v_n}{B_n} \mathbf{B}_t \, , \qquad (3)$$

and thus Eq. (2) becomes:

$$\frac{\mathrm{d}H_A}{\mathrm{d}t} = -2 \int_{\mathcal{S}} (\mathbf{A}_p \cdot \mathbf{u}) B_n \; \mathrm{d}\mathcal{S} \, , \qquad (4)$$

where the subscript A indicates that the flux is computed using the vector potential $\mathbf{A}_p$.

1.3. Helicity flux densities

It appears natural to define a helicity flux density, G_A, as the integrand of Eq. (4):

$$G_A(\mathbf{x}) = -2(\mathbf{A}_p \cdot \mathbf{u}) B_n \, . \qquad (5)$$

G_A has been used in several studies to determine the spatial injection patterns of magnetic helicity in active region (e.g. Chae 2001; Chae et al. 2001, 2004; Kusano et al. 2002, 2004a,b; Maeshiro et al. 2005; Moon et al. 2002a,b, 2003a,b; Nindos & Zhang 2002; Nindos et al. 2003; Yamamoto et al. 2005; Yokoyama et al. 2003). In all these different works, G_A maps always appear extremely complex both in space and time, with polarities of both signs present at any time.

However, in a recent work (Pariat et al. 2005) we showed that G_A is not a real helicity flux density and that its properties introduce artificial polarities of both signs. If G_A produces spurious signals, it is mostly due to the fact that helicity flux densities per unit surface are not physical quantities. Due to the properties of helicity, only helicity flux density per unit of elementary magnetic flux has a physical meaning (see the definition of $\mathrm{d}h_\Phi/\mathrm{d}t$ in Section 5). But to estimate such quantity using real observations, it is necessary to isolate flux tubes and determine their connectivity, which is actually not possible. Thus any definition of a helicity flux density will only be a proxy of the helicity flux density per unit magnetic flux. But some definitions may have properties which do not permit us to estimate the injection patterns of magnetic helicity correctly.

In Pariat et al. (2005), we presented a new estimate of helicity flux density, G_θ, that does not suffer from the same problems as G_A. The helicity flux can be understood as the quantity which measures how the motions of the field lines' footpoints tend to twist, writhe and shear the field lines, i.e. how each magnetic polarity moves relatively to the others. Thus the helicity flux density at a given location is linked to the motions of all elementary flux tubes, relative to the elementary flux tube at that location. It is possible to write the helicity flux as a double integral over the surface which involves the relative rotation rate, $\mathrm{d}\theta(\mathbf{r})/\mathrm{d}t$, of pairs of photospheric positions defined by $\mathbf{x}$ and $\mathbf{x}'$, with $\mathbf{r} = \mathbf{x} - \mathbf{x}'$. For a planar surface one obtains:

$$\frac{\mathrm{d}H_\theta}{\mathrm{d}t} = -\frac{1}{2\pi} \int_{\mathcal{S}} \int_{\mathcal{S}'} \frac{\mathrm{d}\theta(\mathbf{r})}{\mathrm{d}t} \; B_n B'_n \; \mathrm{d}\mathcal{S} \; \mathrm{d}\mathcal{S}' \, , \qquad (6)$$

where the subscript θ indicates that the flux is computed using the relative rotation rate. Then G_θ is simply defined by:

$$G_\theta(\mathbf{x}) = -\frac{B_n}{2\pi} \int_{\mathcal{S}'} \frac{\mathrm{d}\theta(\mathbf{r})}{\mathrm{d}t} \; B'_n \; \mathrm{d}\mathcal{S}' \, . \qquad (7)$$

We compared the properties of G_A and G_θ, applying them to several theoretical models: translational motions of a single polarity, separation and rotation of two polarities, and emergence of a twisted flux tubes (Pariat et al. 2005). In all cases, we showed that G_A almost always produces spurious signals that confuse the interpretation of the injection of helicity. Fortunately, the helicity density maps obtained using G_θ are much closer to the expected helicity flux patterns. Although G_θ produces some fake signals for some configurations, these parasitic helicity flux density polarities are much fainter than with G_A. In the case of the emergence of a twisted flux tube, we estimated that these spurious polarities mask the real injected helicity flux when the number of turns of the twisted flux tube is lower than a few tenths of a turn (the flux tube being represented by half a torus). With G_θ the threshold in the number of turns is ten times lower than with G_A. Thus with G_θ we should be able to correctly analyze the injection of helicity of flux tubes whether they have small, medium, or large twist.

1.4. Aims of this paper

From our previous theoretical analysis we concluded that G_θ is much better suited for determining the patterns of helicity injection. But is it true with real observations? In observations of G_A , are the patchy structures of positive and negative sign fake polarities induced by G_A or are they real signals? If they are real injections then G_A and G_θ maps should be similar. Even if our theoretical analysis argues that G_θ is better, parameters such as the size of the magnetic polarities, the helicity they carry, the velocity of the photospheric motions involved in complex active regions, may be such that G_A could account for the real injection of magnetic helicity. If not, one would observe different patterns between G_θ and G_A maps. In such case the obvious questions are: (1) can we understand the injection of helicity directly from G_θ maps? (2) does G_θ also produce fake polarities that mask the real injection pattern ?

In order to address these questions, in this paper we compare G_A and G_θ maps of the active regions (ARs) previously studied by Nindos et al. (2003). The data are described in Section 2. Section 3 presents the differences in the helicity density maps leading to a completely new view of the structure of the helicity injection in ARs. In Section 4 we compare the total helicity fluxes derived from the two different definitions of helicity flux density. Then we give examples of the limitations of G_θ (Section 5). Finally in Section 6 we present conclusions about the main implications of the re-interpretation of helicity injection pattern for the subphotospheric physics and coronal activity.

2. Data and methods

2.1. Magnetic data

We studied five active regions, namely AR 8210, AR 8375, AR 9114, AR 9182 and AR 9201. The details about these active regions, in particular the time evolution of their magnetic and velocity field as well as their eruptivity are presented by Nindos et al. (2003). In summary, all of them were associated with several major flares and CMEs. AR 8210, AR 8375 and AR 9114 were formed of one large concentrated magnetic polarity with the opposite polarity being much more dispersed. AR 9182 appeared as a bipolar active region and presented significant flux emergence near the leading spot. AR 9201 was a decaying active region, with both polarities decaying similarly. We used 1-minute cadence and 96-minute cadence MDI data. The 1-minute cadence data were available at the time intervals indicated in Table 1 in Nindos et al. (2003). These data consist of both high-resolution images (pixel size of 0.6") and full-disk images (pixel size of 2"). Since MDI magnetograms data suffer from instrumental effects (Berger & Lites 2003; Nindos & Zhang 2002), we corrected all MDI fluxes as detailed in Nindos et al. (2003). Since we we do not want to include solar rotation in the computations of helicity injection (which is in any case negligible, see Démoulin et al. 2002), we removed solar differential rotation, taking as reference time the time when the active region passes through the central meridian.

2.2. Derivation of G_A

In order to compute G_A (Eq. 5), three quantities must be derived from observations. First one needs to know B_n. The MDI data provide only the longitudinal (along the line of sight) component of the magnetic field and we assume that the photospheric magnetic field is vertical. The vertical field component is then directly equal to the longitudinal field divided by the cosine of the heliocentric angle of the active region. The estimation of the errors induced by this approximation is presented in Nindos et al. (2003).

Then the vector potential of the potential field, $\mathbf{A}_p$, needs to be computed. $\mathbf{A}_p$ is derived from B_n, following Chae (2001). In order to avoid boundary effects when using the fast Fourier transform, each original magnetogram has been placed at the center of a map which is 2-3 times bigger, and 2048 × 2048 modes were used.

The last quantity which is required to compute G_A is $\mathbf{u}$, the velocity of the footpoints of the flux tubes. $\mathbf{u}$ can be directly estimated by applying the LCT method to the longitudinal magnetograms. The errors and limitations induced by the LCT are discussed in Démoulin & Berger (2003) and in Section 6 of Nindos et al. (2003). Here the LCT parameters used were $\omega = 7.5''$ for the apodizing window function and $\Delta T = 15 - 20$ minutes for the time interval between a pair of images. Since LCT faces difficulties in regions such as sunspot umbrae, where the spatial variations of the field are small, we used white-light images and not the magnetograms to determine the velocity fields in the umbrae and penumbrae of sunspots.

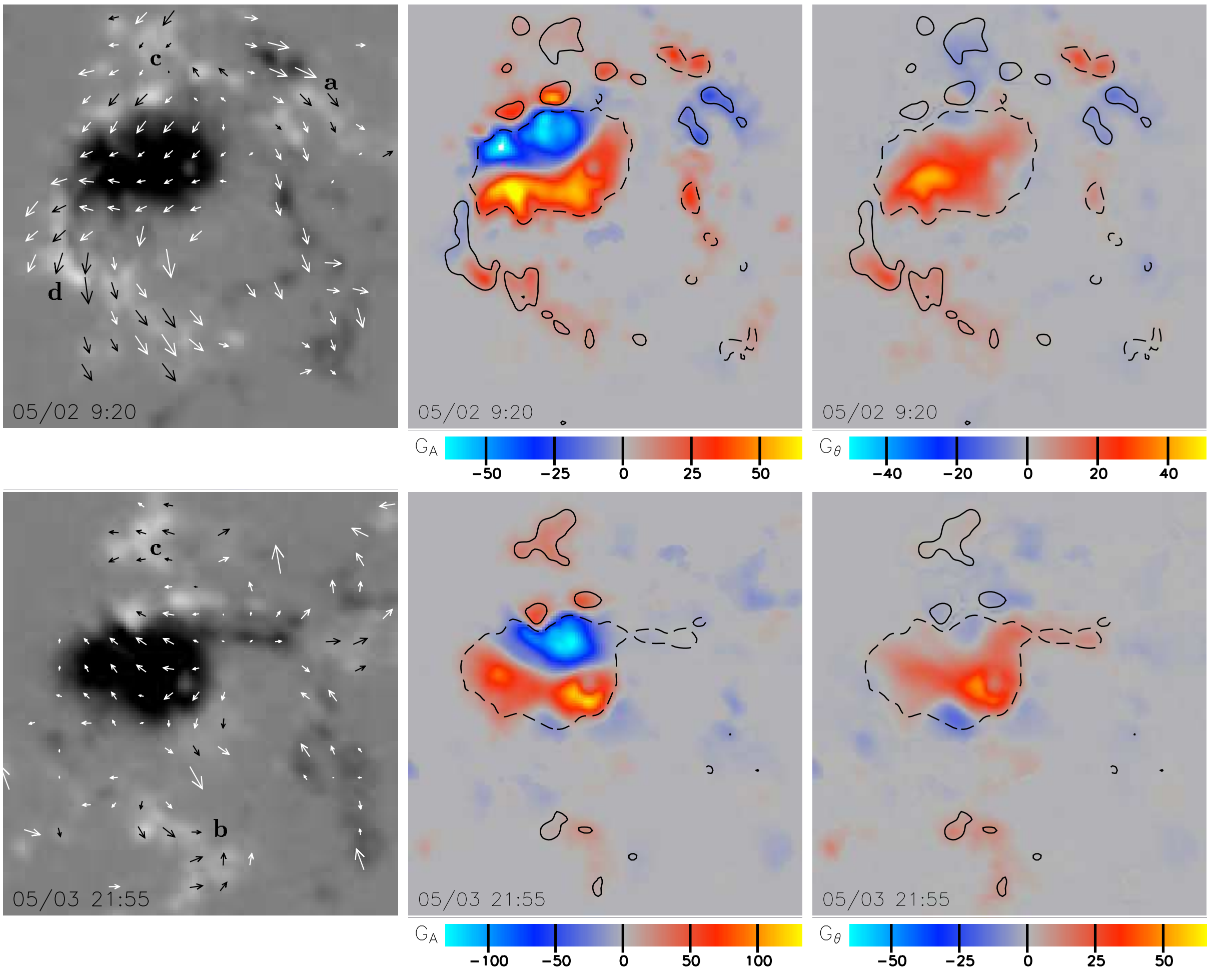

Fig. 1. AR 8210 at 09:20 UT on May 2, 1998 (top) and at 21:55 UT on May 3, 1998 (bottom). Left panels: B_n magnetograms with velocity field (arrows). Center panels: G_A maps. Right panels: G_θ maps. G_A and G_θ maps are in units of 10^6 Wb^2.m^{-2}.s^{-1} and have ± 300 G isocontours of B_n. Note that the scale is not the same for the G_A and the G_θ maps.

2.3. Derivation of G_θ

To compute G_θ, we only need to know B_n and $\mathbf{u}$. Since the vector potential is not required here, G_θ is not affected by the errors induced by the discrete fourier transform when computing $\mathbf{A}_p$. It is also not necessary to insert the data in a larger map. G_θ can be directly computed from the original data. Since equation (7) involves a double integral over the field of view, computing G_θ may be more CPU-time-consuming than computing G_A. This is why, when studying the evolution of the helicity flux in Section 4, we did not consider all magnetogram pixels to compute $\mathrm{d}H_\theta/\mathrm{d}t$. We only computed it at the pixels where the absolute value of the longitudinal field was higher than 20 Gauss. This allowed us to reduce significantly the computation time with only marginal influence on the computed values of $\mathrm{d}H_\theta/\mathrm{d}t$. Indeed for several cases, we checked that the differences between our results and the derived values when no threshold was used was less than a few percents.

At present no study has yet been done to estimate the influence of noise and systematic errors due to the LCT methods on G_θ. The LCT method limitations adduced by Démoulin & Berger (2003) should nevertheless influence any G_θ estimation. Even if this is an important issue and the subject of a future work, one should note that it is not important in our present study: our aim is here to compare G_θ and G_A using the very same dataset.

3. Helicity flux density maps

Almost all G_A maps presented in recent helicity studies show complex patterns with mixed polarities (Section 1.3). Kusano et al. (2002) concluded that in active regions positive and negative helicity is simultaneously injected, even in unipolar magnetic regions. However we claim here that this is mostly due to fake signals induced by G_A which almost always mask the real injection of helicity. A more trustworthy helicity density, G_θ, indeed shows that the helicity injection patterns are rather uniform in sign. We will demonstrate that through several examples.

3.1. Comparison for AR 8210

AR 8210 has been the subject of several studies (see e.g. Welsch et al. 2004, and references therein) and pro-

Table 1. Total helicity fluxes, $\mathrm{d}H_A/\mathrm{d}t$ (Eq. 4) and $\mathrm{d}H_\theta/\mathrm{d}t$ (Eq. 6) and minimum and maximum values of the helicity flux densities G_A and G_θ. Fluxes are in units of 10^{21} $\mathrm{Wb}^2.\mathrm{s}^{-1}$ and densities in units of 10^6 $\mathrm{Wb}^2.\mathrm{m}^{-2}.\mathrm{s}^{-1}$.

NOAA	Date &	Total flux		G_A		G_θ	
AR	Time (UT)	$\mathrm{d}H_A/\mathrm{d}t$	$\mathrm{d}H_\theta/\mathrm{d}t$	min	max	min	max
8210	98/05/02 09:20	15	14	-69	74	-11	42
	98/05/03 21:55	8.9	13	-134	125	-16	49
8375	98/11/04 06:25	4.4	4.6	-33	52	-10	23
	98/11/05 07:35	7.2	6.5	-35	64	-17	22
9114	00/08/08 03:35	-2.9	-2.4	-26	27	-7.1	5.6
	00/08/09 14:20	-4.2	-4.3	-27	18	-16	5.5
9182	00/10/10 21:40	3.8	4.8	-21	38	-5.2	18
	00/10/11 21:40	1.1	0.9	-20	22	-9.0	13
9201	00/10/22 12:05	0.15	0.12	-8.1	9.1	-3.1	4.2
	00/10/25 09:30	-0.63	-0.68	-8.8	3.5	-1.8	0.8

duced several major flares and CMEs. It presents a δ-configuration with a main negative-polarity spot (Fig. 1). This negative spot shows clockwise flow whereas anticlockwise motions dominate the positive polarities. Figure 1 presents G_θ and G_A maps of AR 8210 at two different times: on May 2, 1998, at 9:20 UT and on May 3, 1998 at 21:55 UT. The G_A maps are dominated by two polarities of opposite sign in the center of the negative magnetic spot. The surrounding positive magnetic polarities are associated with mostly positive injection of helicity. The maximum and minimum values reached by G_A and G_θ are presented in Table 1. The maximum absolute flux density is reached in the negative spot. Note that on May 3, the negative values of G_A reach the strongest absolute values even if the total helicity flux is positive.

The G_θ maps present a completely different pattern than the G_A maps. The negative magnetic polarity here is almost entirely dominated by positive helicity flux density. There are no more strong negative helicity densities. The maximum value of the helicity flux density is thus much smaller in G_θ than in G_A. It is 1.7 times lower on May 2 and 2.6 times lower on May 3. The ratio $\min(G_A)/\min(G_\theta)$ is even more important. It is about 6.1 on May 2 and reaches 7.9 on May 3. Negative polarities become very faint in the G_θ maps and thus the maps are much more homogenous than the G_A maps.

The remnant negative helicity polarities could be real localized injection of negative helicity but could still be spurious signals, this time due to G_θ. With our present data it is not possible to distinguish between these two possibilities; however with a closer analysis sometimes we may obtain some clues as we will show in Section 5. Whatever, these G_θ negative polarities have intensities more than 5 times lower that the G_A ones.

The surrounding magnetic polarities present fewer differences between G_A and G_θ maps than the main polarity. Some regions have their helicity injection patterns unchanged, such as the bipole in the upper-right corner on May 2 (noted **a** in Fig. 1), and the positive magnetic polarities (noted **b**) in the lower part of the May 3 map. Other regions present opposite signs of helicity in G_A and G_θ maps, for example the positive magnetic polarities which are north of the main magnetic polarity (noted **c** in Fig. 1). Some others regions, like the positive magnetic polarities below the main negative magnetic region in the May 2 map (noted **d**), present the same characteristics as the main magnetic polarity: two opposite-sign polarity in G_A and uniform positive injection in G_θ. This complicates the interpretation: it is difficult to discriminate whether there is real injection or whether spurious signals are involved, both with G_A and G_θ. The intensities are nevertheless lower with G_θ than with G_A in these areas, as in the main magnetic polarity.

3.2. Other examples

Similar patterns also appear in the other active regions. As an example in Fig. 2 we present for AR 8375 B_n magnetograms, G_A and G_θ maps on November 4 and 5, 1998. Here the main positive magnetic polarity has a translational motion toward the solar west. The surrounding negative polarities show a divergent motion from the main spot. As in AR 8210, the main magnetic positive spot presents two polarities of G_A with opposite signs whereas the G_θ maps show a more uniform pattern, primarily with positive helicity flux. Here also G_θ mainly reduces the non-dominant flux densities (see minimum and maximum values of G_A and G_θ in Table 1).

Figure 3 presents maps of the two helicity flux densities for AR 9114. Here again, G_A maps present strong polarities of both signs while G_θ maps mostly present injection of negative helicity. For almost all the helicity flux density maps that we analysed - all are presented in Nindos et al. (2003) - G_θ maps appear much more uniform than G_A maps. There are a few exceptions where strong polarities still remain in the G_θ map. But even for these few cases, the bipolar patterns are not located at the same place and have lower intensities than in G_A maps. We will analyse in more detail such an example in Section 5.

In general, in the main magnetic polarities, in particular those which present significant translational motions and little rotational motions over the scale of a magnetic

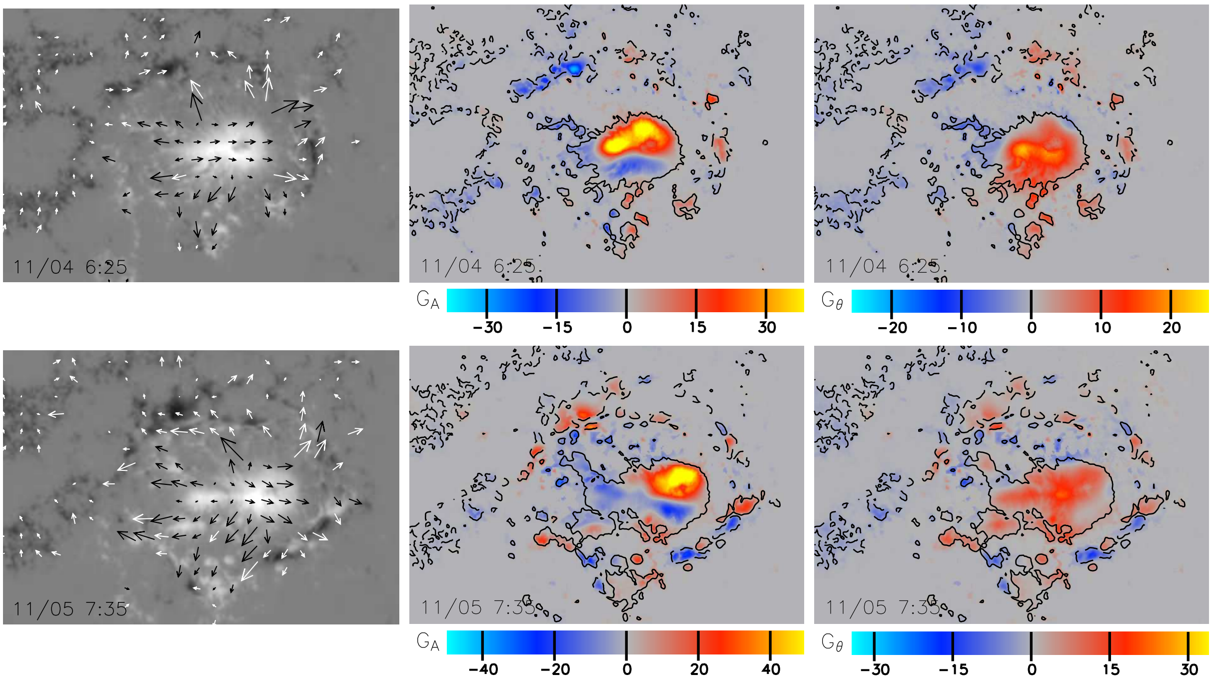

Fig. 2. Same as Fig. 1 but for AR 8375 at 06:25 UT on November 4, 1998 (top) and at 7:35 UT on November 5, 1998 (bottom).

polarity, we found strong polarity of opposite sign in the G_A maps. G_θ substantially reduces the nondominant flux densities: (i.e. polarities with opposite sign to the total injected flux). This is exactly what was expected by Pariat et al. (2005). Since here these signals in G_A tend to disappear in G_θ maps it is clear that the interpretation of observations of helicity flux injection is deeply affected by the fake signals induced by G_A. Even worse, simultaneously with possible injection of real opposite flux, they also create fake polarities of opposite sign whose intensity (in absolute value) may be stronger than the real injected flux. Thus, as we concluded in our previous theoretical study, G_A should not be used as a helicity flux density but rather G_θ should be used (when the magnetic connectivities are not available).

4. Comparison of G_A and G_θ flux

4.1. Total fluxes

Even if G_A and G_θ do not have the same spatial properties, in theory the helicity flux integrated using G_A, $\mathrm{d}H_A/\mathrm{d}t$ (Eq. 4), and using G_θ, $\mathrm{d}H_\theta/\mathrm{d}t$ (Eq. 6) should be strictly equal, because both definitions are derived from Eq. (2).

However, when computing $\mathrm{d}H_A/\mathrm{d}t$ and $\mathrm{d}H_\theta/\mathrm{d}t$, some differences appear. For the 24 G_A maps of the 5 active regions that were presented by Nindos et al. (2003), we found a mean of 0.95 for the ratio between $\mathrm{d}H_A/\mathrm{d}t$ and $\mathrm{d}H_\theta/\mathrm{d}t$ derived using G_θ. The mean absolute deviation of this ratio is equal to 0.25. There is no systematic prevalence of one of these terms over the other and also no dependence on the sign of the helicity flux has been found. Concerning the data used in Figs. 3 and 4, we found that for the 1755 temporal values we considered, the mean ratio of $\mathrm{d}H_A/\mathrm{d}t$ to $\mathrm{d}H_\theta/\mathrm{d}t$ was around 0.94 with mean absolute deviation of 0.26. If we consider the active regions separately we found that for AR 8210 the relative errors between $\mathrm{d}H_A/\mathrm{d}t$ and $\mathrm{d}H_\theta/\mathrm{d}t$ were of the order of a few per cent, while it was around 15% for AR 9114. Nevertheless we note that since there is no significant predominance of one of these two terms over the other, when we time-average the total flux evolution, the difference between $\mathrm{d}H_A/\mathrm{d}t$ and $\mathrm{d}H_\theta/\mathrm{d}t$ becomes very small. This is the reason why we do not present the dH_A/dt time profiles in Figs. 3 and 4: their differences with the dH_θ/dt time profiles are too small to be clearly seen in the figures. For example in AR 8210 the mean absolute deviation of the ratio $\mathrm{d}H_A/\mathrm{d}t$ over $\mathrm{d}H_\theta/\mathrm{d}t$ is 0.19 if one smooths the original data with 2 points and 0.10 if one uses 4 points.

A possible explanation for this discrepancy between these two active regions has to do with their mean helicity fluxes. AR 8210 has a mean absolute helicity flux several times larger than AR 9114 (see Figs. 3 and 4) although AR 8210 magnetic flux is lower than AR 9114 one's (1.6×10^{14} and 3.1×10^{14} Wb respectively). The differences between $\mathrm{d}H_A/\mathrm{d}t$ and $\mathrm{d}H_\theta/\mathrm{d}t$ tend to be smaller when the helicity flux involved is larger. This is probably the effect of noise in the data for the small flux values. Roughly, the differences tend to become important when the helicity flux is lower than 10^{21} $\mathrm{Wb}^2.\mathrm{s}^{-1}$. But these differences may also come from the larger errors in $\mathrm{d}H_A/\mathrm{d}t$ measurement due to the intense fake signals that G_A produces.

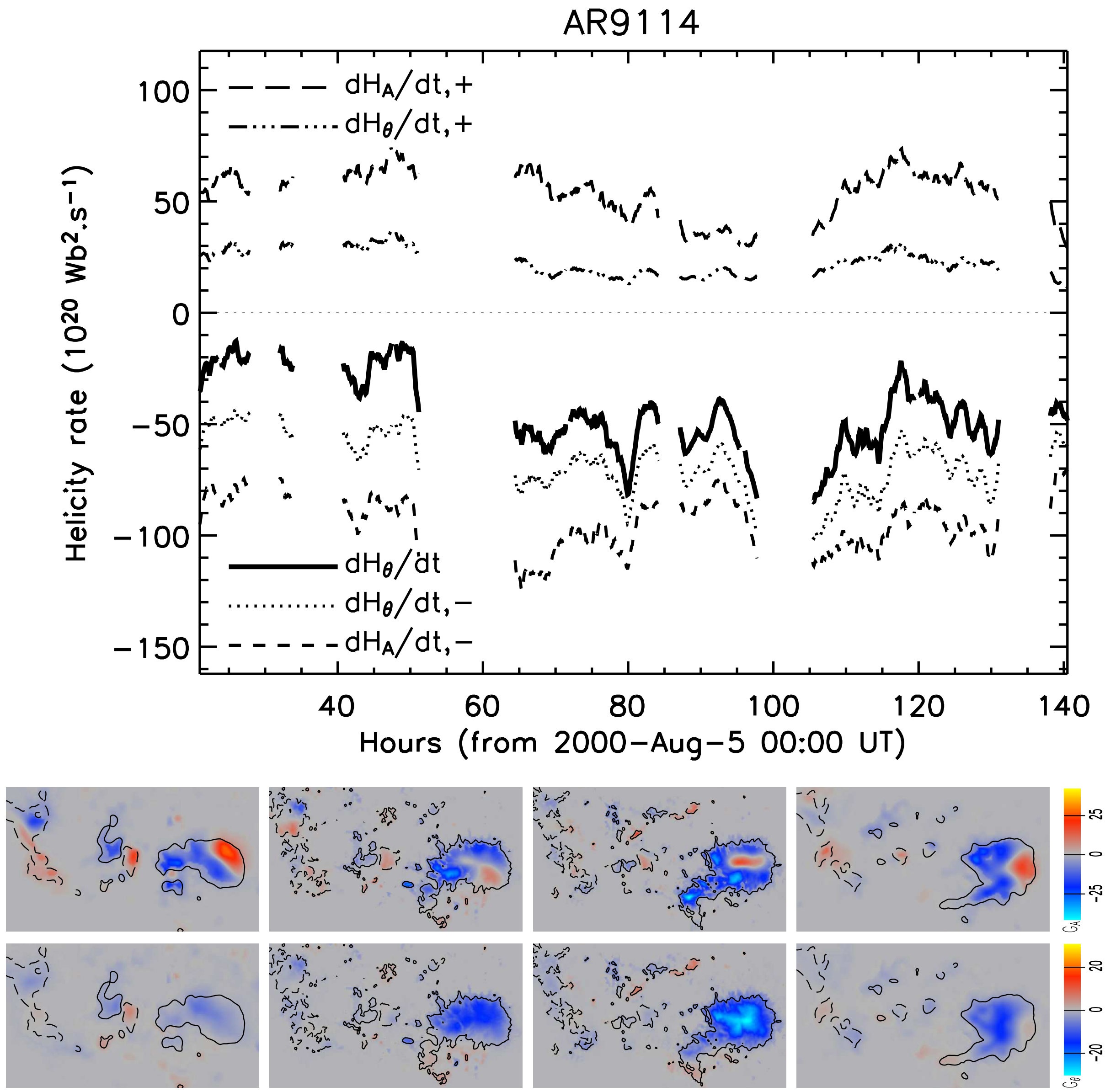

Fig. 3. Upper panel: Plots of $(\mathrm{d}H_A/\mathrm{d}t)_\pm$, $(\mathrm{d}H_\theta/\mathrm{d}t)_\pm$ and $\mathrm{d}H_\theta/\mathrm{d}t$ as a function of time for AR 9114. The curves have been smoothed on a time interval of 100 minutes. We do not present the $\mathrm{d}H_A/\mathrm{d}t$ curve because its differences with respect to the $\mathrm{d}H_\theta/\mathrm{d}t$ curve are too small to be clearly seen. Middle panels and lower panels: G_A and G_θ maps of AR 9114, as in Fig. 1.

4.2. Signed fluxes

Let us define the signed flux $(\mathrm{d}H_A/\mathrm{d}t)_+$ (resp. $(\mathrm{d}H_A/\mathrm{d}t)_-$) as the positive (resp. negative) flux of injected helicity, *i.e.* the sum of G_A over the area where G_A is > 0 (resp. < 0). Let us define $(\mathrm{d}H_\theta/\mathrm{d}t)_+$ and $(\mathrm{d}H_\theta/\mathrm{d}t)_-$ similarly but using G_θ instead of G_A to integrate the flux.

The signed fluxes $|(\mathrm{d}H_A/\mathrm{d}t)_\pm|$ are always larger than $|(\mathrm{d}H_\theta/\mathrm{d}t)_\pm|$, especially the flux with sign opposite to the total injected flux (see Figs 3 and 4). For AR 8210 whose helicity flux is generally positive, $(\mathrm{d}H_A/\mathrm{d}t)_+$ is in average 1.7 times larger than $(\mathrm{d}H_\theta/\mathrm{d}t)_+$ and $|(\mathrm{d}H_A/\mathrm{d}t)_-|$ is 3.0 times larger than $|(\mathrm{d}H_\theta/\mathrm{d}t)_-|$. The negative flux is strongly reduced when using G_θ. In AR 9114 it is still the nondominant flux - the positive flux here - which becomes small when using G_θ. Here $(\mathrm{d}H_A/\mathrm{d}t)_+$ is on average 2.5 times larger than $(\mathrm{d}H_\theta/\mathrm{d}t)_+$ and the mean ratio of $|(\mathrm{d}H_A/\mathrm{d}t)_-|$ over $|(\mathrm{d}H_\theta/\mathrm{d}t)_-|$ is equal to 1.4. In AR 9114 the ratios are smaller than in AR 8210 but this should be due to the fact that the total helicity flux is smaller in AR 9114 and so the noise in G_θ and the fake polarities induced by G_θ have a stronger influence.

With G_A, part of the strong fluxes of positive and negative helicity cancel out when summing over the whole surface, resulting in small total helicity fluxes. But it is not recommended to add quantities of opposite sign whose intensities are much larger than the intensity of the final result. The systematic errors tend to be added, resulting in a larger inaccuracy of the final result. Thus using G_θ should yield more accurate results when computing the total flux.

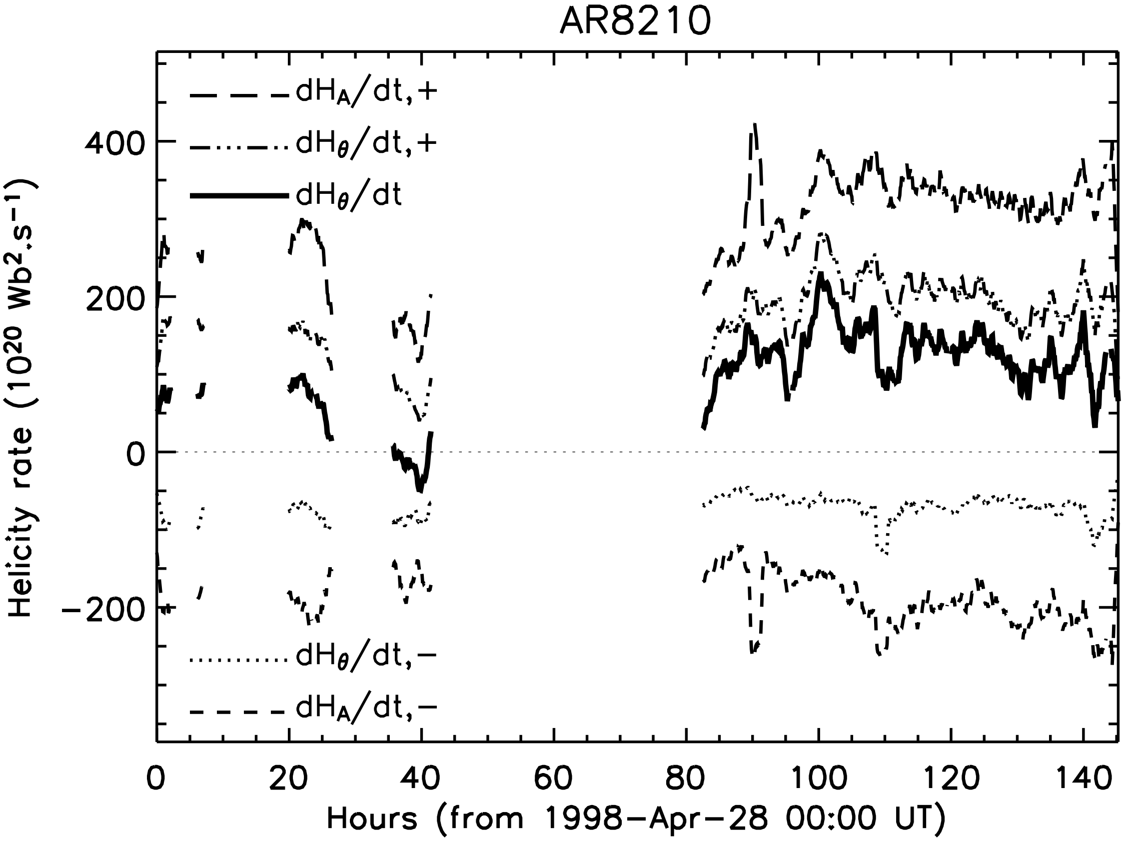

Fig. 4. Plots of $(\mathrm{d}H_A/\mathrm{d}t)_\pm$, $(\mathrm{d}H_\theta/\mathrm{d}t)_\pm$ and $\mathrm{d}H_\theta/\mathrm{d}t$ as functions of time for AR 8210. The curves have been smoothed on a time interval of 100 minutes. Again as in Fig. 3, we do not present the $\mathrm{d}H_A/\mathrm{d}t$ curve because its differences with respect to the $\mathrm{d}H_\theta/\mathrm{d}t$ curve are too small to be clearly seen.

4.3. Time evolution of fluxes

Another important feature with G_θ is that the study of the temporal evolution of helicity flux injection becomes much more simple. The lower panels of Fig. 3 present G_A and G_θ maps at four different times. It is directly possible to follow qualitatively the evolution of the total helicity flux by visual inspection of the G_θ maps; for example in this case there is an increase of negative helicity and then a decrease. This evolution is not that apparent in the G_A maps. The reason why the overall evolution can be directly inferred from the G_θ maps is mostly due to the fact that the sign of the real injection of helicity is uniform.

The fluctuations of the total and signed fluxes are also strongly reduced with G_θ compared to those with G_A. For example, in AR 9114, $(\mathrm{d}H_A/\mathrm{d}t)_+$, $(\mathrm{d}H_A/\mathrm{d}t)_-$ and dH_A/dt present standard deviations of 3.5, 7.3, and 8.9 $\times 10^{21}$ Wb^2.s^{-1} respectively, while the standard deviations of $(\mathrm{d}H_\theta/\mathrm{d}t)_+$, $(\mathrm{d}H_\theta/\mathrm{d}t)_-$, and dH_θ/dt are 0.8, 1.6, and 2.4 $\times 10^{21}$ Wb^2.s^{-1} respectively (these results are obtained with the time cadence ΔT of the LCT, see Section 2.3).

We also remark that with G_θ, the nondominant flux is relatively constant (see the $(\mathrm{d}H_\theta/\mathrm{d}t)_+$ curve of Fig. 3 and the $(\mathrm{d}H_\theta/\mathrm{d}t)_-$ curve of Fig. 4). For example in AR 8210 the mean and the standard deviation of $(\mathrm{d}H_\theta/\mathrm{d}t)_-$ are respectively -6.5 $\times 10^{21}$ Wb^2.s^{-1} and 2.0 $\times 10^{21}$ Wb^2.s^{-1} compared to 19.2 $\times 10^{21}$ Wb^2.s^{-1} and 6.5 $\times 10^{21}$ Wb^2.s^{-1} for $(\mathrm{d}H_\theta/\mathrm{d}t)_+$. This quasi-constant flux strongly questions the real origin of the nondominant signals. Possible reasons for the remnant nondominant helicity flux in G_θ maps could be the noise in the data and also the residual fake polarities that G_θ creates (see Section 5). Thus the intensity of these nondominant fluxes gives an idea of the accuracy on the total flux estimation: $< |(\mathrm{d}H_\theta/\mathrm{d}t)_-| >= 6.5 \times 10^{21}$ Wb^2.s^{-1} in AR 8210 and $< (\mathrm{d}H_\theta/\mathrm{d}t)_+ >= 2.1 \times 10^{21}$ Wb^2.s^{-1} in AR 9114. These values are consistent with the fluctuations of the total helicity flux in non-flaring AR estimated about 3.2 $\times 10^{21}$ Wb^2.s^{-1} by Hartkorn & Wang (2004).

Instead of the total net flux $\mathrm{d}H_A/\mathrm{d}t$, Maeshiro et al. (2005) have used the absolute flux (also called total unsigned flux), defined as the difference between the positive flux and the negative flux. They correlated the absolute helicity flux with X-ray activity. Nevertheless, most of the signals in G_A are in fact spurious signals and are not linked to real helicity injection. Since G_A produces stronger spurious signal when significant translatory motions are involved, the absolute helicity flux is a rather complex tracer of the photospheric field dynamics.

5. Towards better helicity density maps

5.1. G_θ fake polarities

Even if G_θ is not so strongly inclined to produce spurious signals as G_A, we have seen in Sections 3 and 4 that some fake polarities still remain. In previous examples, these G_θ fake polarities had small intensity compared to the main real helicity flux. However there are still some cases where the fake polarities of G_θ may remain dominant and corrupt the interpretation of the patterns of helicity flux. Figure 5 shows such an example.

Before October 9, 2000, AR 9182 consisted of a positive compact leading sunspot and a more extended trailing negative spot. From October 9, magnetic flux emergence occurs west of the active region, in the form of two separating oppositely-signed magnetic polarities (the evolution of this active region is presented in Fig. 7 of Nindos et al. 2003). The original leading sunspot is the positive magnetic polarity noted as P_1 in Fig. 5 whereas the magnetic polarities of the emerging flux are indicated as N_2 and P_2. Since the AR was not close to disk center (N02 E46 on October 11), some longitudinal field reversal due to projection effects appear west of P_2. We will not take that area into consideration.

The G_A map (top left in Fig. 5) presents its usual complex patterns with several helicity flux polarities of both signs. In the G_θ map most of these patchy patterns have disappeared. There are three main areas of uniform flux sign on the three main magnetic polarities: P_2 presents a wide negative G_θ whereas N_2 and P_1 have positive G_θ.

Table 1 presents the minimum and maximum intensities of G_A and G_θ . Here also G_θ reduces the fake polarities induced by G_A. The fluxes involved here are 41,−35 and 6.1×10^{21} $\mathrm{Wb}^2.\mathrm{s}^{-1}$ for $(\mathrm{d}H_\theta/\mathrm{d}t)_+$, $(\mathrm{d}H_\theta/\mathrm{d}t)_-$ and $\mathrm{d}H_\theta/\mathrm{d}t$ respectively. Here both positive and negative fluxes are very strong compared to the total flux and G_θ presents fluxes as strong as G_A, but their spatial distribution is different. Using the G_θ map, one would conclude that there is simultaneous injection of helicity of both signs in the emerging flux (N_2P_2). But is this true?

5.2. Defining a better flux density

In Pariat et al. (2005), we found that only the helicity flux density per elementary flux tube (or per unit magnetic flux) could be defined. Let $\mathrm{d}h_\Phi/\mathrm{d}t|_e$ denote the helicity injected in the elementary flux tube e through its footpoints on the photosphere. Only this helicity flux per unit magnetic flux has a physical meaning.

Nevertheless, it is possible to represent this quantity as a helicity flux density per unit surface by distributing it between the footpoints of the elementary flux tube (whose positions are denoted as $\mathbf{x}_{e_-}$ and $\mathbf{x}_{e_+}$). Each proxy for the helicity flux density is only a way of distributing $\mathrm{d}h_\Phi/\mathrm{d}t|_e$, following some particular “rules”. For example $\mathrm{d}h_\Phi/\mathrm{d}t|_e$ can be related to G_A with the relation:

$$\left.\frac{dh_\Phi}{dt}\right|_e = \frac{1}{2}\left(\frac{G_A(\mathbf{x}_{e_+})}{|B_n(\mathbf{x}_{e_+})|} + \frac{G_A(\mathbf{x}_{e_-})}{|B_n(\mathbf{x}_{e_-})|}\right) - \frac{1}{2\pi}\int_{\mathcal{S}'} \mathbf{u}' \times \left(\frac{\mathbf{x}'-\mathbf{x}_{e_+}}{(\mathbf{x}'-\mathbf{x}_{e_+})^2} - \frac{\mathbf{x}'-\mathbf{x}_{e_-}}{(\mathbf{x}'-\mathbf{x}_{e_-})^2}\right) B'_n \,\mathrm{d}\mathcal{S}' \,. \quad (8)$$

This equation is quite complex since G_A fails to measure the net rotation of the dipole $(\mathbf{x}_{e_+}\mathbf{x}_{e_-})$ over the photospheric field. With G_θ the link is much more direct :

$$\left.\frac{dh_\Phi}{dt}\right|_e = \frac{G_\theta(\mathbf{x}_{e_+})}{|B_n(\mathbf{x}_{e_+})|} + \frac{G_\theta(\mathbf{x}_{e_-})}{|B_n(\mathbf{x}_{e_-})|} \,. \quad (9)$$

$\mathrm{d}h_\Phi/\mathrm{d}t|_e$ is simply a field-weighted average of G_θ at both footpoints, and thus can be estimated using G_θ (provided that the field line connectivity is known).

Now, let us go back to AR 9182 where (N_2 P_2) is emerging. If we suppose that they are still completely magnetically connected and that they form a single flux tube then the real helicity flux injected in this flux tube will be the sum of the helicity injected through N_2 and P_2. But since they have opposite values of G_θ with similar absolute intensities, the sign of $\mathrm{d}h_\Phi/\mathrm{d}t$ cannot be directly deduced. Even if intense signals of G_θ are present, the real injected helicity is much weaker. This is why here G_θ fails to give an accurate picture of the real patterns of injected helicity. For this particular case, the properties of G_θ distribute the helicity per unit magnetic flux over the footpoints in such a way that large fake polarities appear.

The best surface helicity flux density proxies of dh_Φ/dt, can be obtain by sharing dh_Φ/dt equally between the two footpoints of each field line. One can use G_Φ, defined as (derived from Eq. 29 of Pariat et al. 2005,with f=1/2):

$$G_\Phi(\mathbf{x}_{e_\pm}) = \frac{1}{2}\left(G_\theta(\mathbf{x}_{e_\pm}) + G_\theta(\mathbf{x}_{e_\mp})\left|\frac{B_n(\mathbf{x}_{e_\pm})}{B_n(\mathbf{x}_{e_\mp})}\right|\right) . \quad (10)$$

5.3. Helicity flux densities with a model

In the ARs that we have analyzed it was not possible to determine the field line linkage. But in order to have an idea of what G_Φ would give for AR 9182, we can model this active region with two flux tubes having torus shape and the same small radius and field strength. The distribution of the field perpendicular to the torus axis is assumed to be constant. The photospheric feet of the first flux tube corresponds to the original pre-existing polarity. The second half torus flux tube models the emerging magnetic flux (N_2 P_2). The model flux tubes are not twisted.

We implemented four kind of motions for these polarities to describe the main velocity pattern observed in AR 9182. First, we considered a vertical emergence of the second flux tube. Second, we also imposed an eastward translational motion on that emerging flux tube, so that P_2 does not present any east-west motion. Third, we considered a solid rotation of this whole flux tube, relatively to N_2. Finally, for the first flux tube, we only considered a translation toward the west. Observed and modelled $\mathbf{u}$

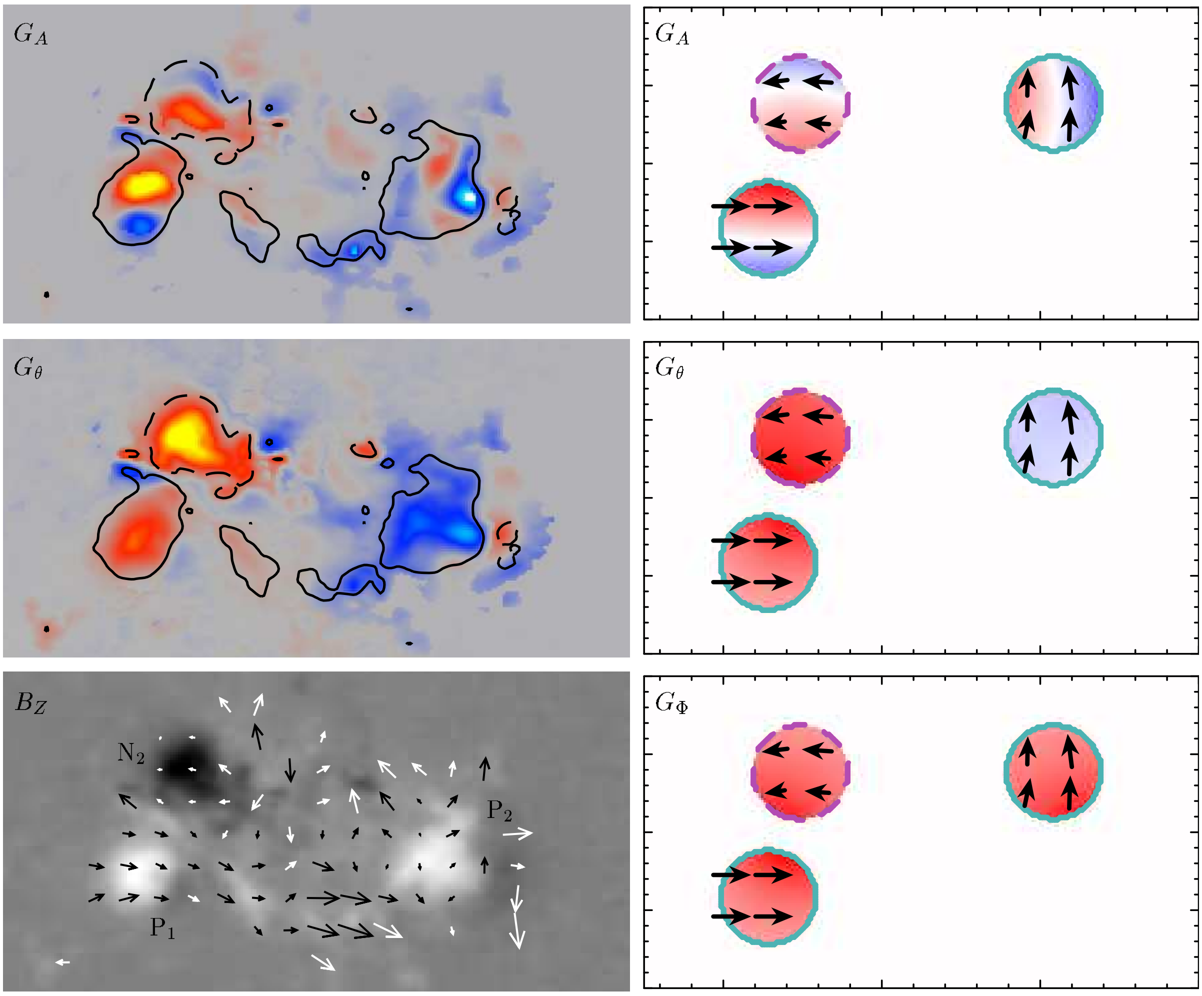

Fig. 5. Left: AR 9182 on October 11, 2000 at 21:40 UT: G_A map (top panel), G_θ map (middle panel) and B_Z magnetogram (bottom panel). The B_Z isocontours on the observations maps are for $B_Z = \pm 300$ G. Right: Model maps of helicity flux densities; G_A (top panel), G_θ (middle panel) and G_Φ (bottom panel). The isocontours in the model maps are the ones used for the B_Z data.

fields (Eq. 3) are compared in Fig. 5. For simplicity, these torus-like flux tubes are represented when they are almost half-emerged, thus the sections of the tubes appear as circles, of opposite polarities.

We adjusted the relative intensities of the motions, in order to make a better correspondence between the observations and model, matching not only the velocity field but also the G_A and G_θ patterns. With the above simple model we are able to derive both G_A and G_θ having the same main features as the observed maps. In particular the main polarities of G_A in AR 9182 are reproduced by the model. The model G_θ map, shows that negative density is located in P$_2$ whereas positive helicity flux appears in N$_2$ and P$_1$. P$_1$ present the largest helicity flux, as in the observations.

The G_Φ map (bottom right in Fig. 5) gives a different result: the three magnetic polarities present positive helicity density. Among the evolution motions we considered, we found that the translational motion and the emergence are responsible for positive helicity injection while only the solid rotational motion of the emerging polarities is a source of negative helicity. With the considered relative intensities for each motion, the positive helicity dominates the helicity flux, the main source of helicity being the translational motions.

Indeed mutual helicity is injected in both tubes due to the relative displacement of each tube with respect to the other. In particular the emergence of an untwisted flux tube nearby another one leads to injection of helicity in both tubes. This may appear paradoxical if one considers two untwisted closed rings of magnetic flux which are not linked. No matter what kind of motions we apply to them (if there is no modification of the linking number) their helicity should remain null. But when computing the relative helicity flux through a boundary which intersects these rings, one observes some helicity flux. This injection is mainly due to the apparent motion of the footpoints of the rising torus. Since the helicity flux changes sign when the torus is half emerged (the footpoint motion reverse), the total helicity injected will be null when the torus will be completely emerged, and so the paradox disappears. Also note that the injection of opposite signs of G_θ to the two polarities of the torus footpoints depends on the distance to the second flux tube (to the right of the panels in figure 5). The maximum effect occurs when this distance is approximately equal to the distance between the two torus footpoints.

If the emerging flux tube is twisted, the helicity flux due to the self-helicity may only appear if the twist is large enough to dominate this mutual helicity effect. In our model the mutual helicity injection will dominate if the number of turns for half the torus is lower than 0.002, so only for very weakly twisted flux tubes. Since G_A and G_θ patterns found for AR 9182 and for the model are qualitatively similar, this is an indication that the helicity flux density obtained for AR 9182 is dominated by the mutual helicity. Indeed, there is no evidence of twisting motions in the deduced LCT motions. We conclude that the LCT was only able to detect the relative motions of the magnetic polarities (and could have missed the internal motions).

6. Conclusion/Discussion

6.1. Results

In Pariat et al. (2005), we demonstrated how the usual proxy of magnetic helicity flux density, G_A, can produce spurious signals, and we defined two new proxies of helicity flux density: G_θ and G_Φ. G_Φ is the most accurate definition, but G_θ is practically more appropriate to work with observational data because G_Φ requires the knowledge of the field line connectivity. The present paper addresses the application of G_θ to real observations in comparison with G_A. We have applied G_θ to the same set of data that were studied by Nindos et al. (2003), in which G_A was used.

The comparison of G_A and G_θ maps shows that G_A indeed creates strong fake polarities, due to the translational motions of magnetic polarities (Sect. 3). With G_θ these spurious signal disappear: the nondominant polarities of the helicity flux are suppressed and the intensities of the predominant polarities are lowered. The real injection pattern of magnetic flux can now be examined. For all five active regions that we studied, the pattern of the helicity injection is much more homogeneous in G_θ maps than in G_A maps. For most ARs, even if some nondominant polarities are still present in the G_θ maps, their intensities are much smaller than the intensities of the main helicity flux density polarities. Furthermore, it is not obvious whether these nondominant polarities are real signal, noise or spurious signal due to G_θ.

The total and signed helicity flux computed using G_A and G_θ were also compared. One expects that the total fluxes should be equal, but some differences do exist between $\mathrm{d}H_A/\mathrm{d}t$ and $\mathrm{d}H_\theta/\mathrm{d}t$ in our data (Sect. 4.1). Theses differences do not have a preferential sign and thus tend to become very small when the data are time-averaged. The relative differences are also somewhat stronger when the total fluxes are small in absolute value. Concerning the unsigned fluxes, the nondominant helicity flux with G_θ is strongly reduced compare with G_A (Sect. 4.2). In the two active regions for which we computed the time evolution, the total flux is mainly due to the evolution of the dominant signed flux in G_θ. The nondominant flux appears to be roughly constant. This may give an estimation of the intensities of the fake polarities that G_θ generates (Sect. 4.3) and an indication about the noise level in the computation of the total helicity flux.

Indeed, although G_θ reduces efficiently spurious signals induced by G_A, G_θ can also present fake polarities. AR 9182 is likely to be an example where G_θ creates intense unreal polarities (Sect. 5.1). In fact only the helicity flux density per elementary flux tube, dh_Φ/dt, is physically meaningful and G_Φ is the best proxy for it (Sect. 5.2). It is nevertheless difficult to use such quantity since it is necessary to determine the coronal linkage to compute G_Φ, which is presently not possible. In practice, G_θ is the best and most simple solution for mapping the injection of helicity. Even if it may induce spurious signals in some cases it is possible to infer the real patterns. For example, when two oppositely signed magnetic polarities which are believed to be linked present opposite G_θ signs, the real helicity flux is an average of the helicity densities at these magnetic polarities as shown in Fig. 5. In the case of AR 9182, as predicted, the negative G_θ polarity in P_2 is only a fake signal if one supposes that P_2 and N_2 are linked (Sect. 5.3). Another similar (but less prominent) example appears in the upper right corner of Fig. 1 since the time evolution of the magnetograms shows that the magnetic bipole labeled (**a**) has just emerged. Thus even if G_θ sometimes produces fake signals, by a careful analysis, it is still possible to overcome this problem. Moreover, spurious G_θ signals are generally related to weak helicity flux density polarities.

Regarding the pattern of the magnetic helicity injection we found that the helicity flux density distribution is much more homogeneous than previously thought. The patchy structures appearing in helicity flux density maps presented in previous studies (Section 1.3) are likely to come from fake polarities due to the use of G_A. The real injection pattern revealed by G_θ is almost unipolar for most of the active regions that we studied here. From the 28 G_θ maps that we studied only 3 presented opposite sign polarities with intensities of the same magnitude. However in these cases, one may speculate that these patterns are formed primarily by fake polarities due to G_θ as we have demonstrated for AR 9182 where the real injection pattern should be unipolar. Then we concluded that the scale for the helicity flux density polarities is at least of the order of the magnetic polarities if not of the scale of the whole active region.

6.2. Implications of the results

The result of the homogeneous injection of magnetic helicity has implications in three domains.

The photospheric injection is a consequence of the generation of magnetic helicity in the solar interior and of its transport in the convection zone. The cyclonic convection (α-effect), which is thought to be the source of magnetic helicity of active regions, produces simultaneously positive and negative magnetic helicity but with a spectral segregation (Ji 1999). Brandenburg & Blackman (2002) argue that magnetic helicity at different scales, and thus of different sign, must have different behaviors. The observed unipolar injection of magnetic helicity would define constraints for such models. However it is worth to keep in mind that presently the LCT method is efficient to detect motions of magnetic polarities (and mostly translatory motions) only on scales larger than the apodizing window. Refined methods to determine the velocity field are needed to improve the observational constraints; some are in development (Schuck 2005).

The injection of helicity with uniform sign has also some implications on some models of solar flare triggering. Kusano et al. (2004b) developed a mechanism based on the annihilation of opposite-sign magnetic helicity. This model was mostly based on the observations of mixed sign helicity injection. Even if one does not question the validity of their model, at least the scales and the frequencies for its application have to be studied. In order to test this model with observations it is important to remove as much as possible the fake polarities. Statistical studies of the real helicity injection pattern - using G_θ and possibly G_Φ - linked to eruptive events must be performed.

Finally the injection of magnetic helicity with uniform sign supports the idea that CMEs are the way for the solar atmosphere to eject helicity (which cannot accumulate forever) (Rust 1994; Low 1996), and further that CMEs appear after sufficient amount of magnetic helicity has been stored (Nindos & Andrews 2004). Regular, uniform, unipolar helicity flux through the photosphere slowly increases the absolute total coronal magnetic helicity of an active region, which will then have to eject it in CMEs.

Acknowledgements. A N acknowledges financial support from the Greek Ministry of Education's "Pythagoras II" grant.

References

Berger, M. A. 2003, Topological quantities in magnetohydrodynamics (Advances in Nonlinear Dynamics), 345–383
Berger, M. A. & Field, G. B. 1984, J. Fluid. Mech., 147, 133
Berger, T. E. & Lites, B. W. 2003, Sol. Phys., 213, 213
Brandenburg, A. & Blackman, E. G. 2002, in ESA SP-506: Solar Variability: From Core to Outer Frontiers, 805–810
Brown, M., Canfield, R., & Pevtsov, A. 1999, Magnetic Helicity in Space and Laboratory Plasmas (Geophy. Mon. Ser. 111, AGU)
Chae, J. 2001, ApJ, 560, L95
Chae, J., Moon, Y., & Park, Y. 2004, Sol. Phys., 223, 39
Chae, J., Wang, H., Qiu, J., et al. 2001, ApJ, 560, 476
Démoulin, P. & Berger, M. A. 2003, Sol. Phys., 215, 203
Démoulin, P., Mandrini, C. H., van Driel-Gesztelyi, L., et al. 2002, A&A, 382, 650
Finn, J. H. & Antonsen, T. M. 1985, Comments Plasma Phys. Contr. Fusion, 9, 111
Hartkorn, K. & Wang, H. 2004, Sol. Phys., 225, 311
Ji, H. 1999, Physical Review Letters, 83, 3198
Kusano, K., Maeshiro, T., Yokoyama, T., & Sakurai, T. 2002, ApJ, 577, 501
Kusano, K., Maeshiro, T., Yokoyama, T., & Sakurai, T. 2004a, in Astronomical Society of the Pacific Conference Series, 175
Kusano, K., Maeshiro, T., Yokoyama, T., & Sakurai, T. 2004b, ApJ, 610, 537
Kusano, K., Yokoyama, T., Maeshiro, T., & Sakurai, T. 2003, Advances in Space Research, 32, 1931
Low, B. C. 1996, Sol. Phys., 167, 217
Maeshiro, T., Kusano, K., Yokoyama, T., & Sakurai, T. 2005, ApJ, 620, 1069
Moon, Y.-J., Chae, J., Choe, G. S., et al. 2002a, ApJ, 574, 1066
Moon, Y.-J., Chae, J., & Park, Y. D. 2003a, Journal of Korean Astronomical Society, 36, 37
Moon, Y.-J., Chae, J., Wang, H., Choe, G. S., & Park, Y. D. 2002b, ApJ, 580, 528
Moon, Y.-J., Chae, J., Wang, H., & Park, Y. D. 2003b, Advances in Space Research, 32, 1953
Nindos, A. & Andrews, M. D. 2004, ApJ, 616, L175
Nindos, A. & Zhang, H. 2002, ApJ, 573, L133
Nindos, A., Zhang, J., & Zhang, H. 2003, ApJ, 594, 1033
Pariat, E., Démoulin, P., & Berger, M. A. 2005, A&A, 439, 1191
Rust, D. M. 1994, Geophys. Res. Lett., 21, 241
Schuck, P. W. 2005, ApJ, 632, L53
Welsch, B. T., Fisher, G. H., Abbett, W. P., & Regnier, S. 2004, ApJ, 610, 1148
Yamamoto, T. T., Kusano, K., Maeshiro, T., Yokoyama , T., & Sakurai, T. 2005, ApJ, 624, 1072
Yokoyama, T., Kusano, K., Maeshiro, T., & Sakurai, T. 2003, Advances in Space Research, 32, 1949